Overlayer Surface-Enhanced Raman Spectroscopy for Studying the Electrodeposition and Interfacial Chemistry of Ultrathin Ge on a Nanostructured Support

Azhar I. Carim,[†] Junsi Gu,[†] and Stephen Maldonado[†,‡,*]

[†]Department of Chemistry and [‡]Program in Applied Physics, University of Michigan, 930 North University Avenue, Ann Arbor, Michigan 48109-1055,United States

Nanostructured germanium (Ge) is ideally suited for next generation, high speed optoelectronic devices.[1] Crystalline Ge natively has large carrier mobilities and the large Bohr exciton radius of Ge[2] affords a high degree of tunability in the electrical and optical properties of nanostructured and thin film Ge materials.[3,4] Ge-based nanomaterials currently are being developed for fast photodetectors,[5,6] efficient multijunction photovoltaics,[7] and nonvolatile memory devices.[8] To integrate Ge into these and related technologies, better control and understanding of deposition processes with high fidelity are required. As industrial device fabrication processes typically rely on wet chemical cleaning procedures, the instability of Ge interfaces and the lack of high-quality and stable oxide passivation layers have severely hindered the maturation and implementation of Ge-based optoelectronics. A more detailed, molecular-level understanding of the reactivity of Ge interfaces is accordingly needed. To this end, new and improved strategies for studying and monitoring nanostructured Ge materials and their interfaces must be identified and developed.

Although several established spectroscopic techniques have been used to study Ge materials and their interfaces in detail, each method has definable limitations. Traditional ultrahigh vacuum (UHV) surface-sensitive spectroscopies such as X-ray photoelectron and electron energy loss spectroscopy do not provide information in real time, under ambient or application-relevant conditions. Even considering advances in high-pressure X-ray spectroscopic techniques,[9,10] *in situ* measurements during the course of a wet chemical process are not feasible. Although vibrational spectroscopic methods such as sum frequency generation spectroscopy, Brewster-angle transmission infrared (IR) spectroscopy, and reflectance-based IR spectroscopies can provide detailed vibrational information in reactive media, these techniques are best suited for optically flat, planar interfaces and cannot be used to study low frequency signals (<600 cm^{-1}) that are typical for phonon modes and adsorbate stretches. In this regard, surface-enhanced Raman spectroscopy (SERS) has long been identified as a

ABSTRACT Ultrathin films of germanium (Ge) have been electrodeposited onto surface-enhanced raman spectroscopy (SERS)-active, polycrystalline gold (Au) nanoparticle film electrodes from aqueous solutions containing dissolved GeO$_2$. An overlayer SERS strategy was employed to use the SERS-activity of the underlying Au electrode to enhance the Raman signatures separately for the Ge phonon mode and vibrational modes of surface groups. Electrochemical and spectroscopic data are presented that demonstrate monolayer-level detection of the electrodeposited material and the preparation of crystalline Ge films exhibiting quantum-confinement effects. Potential-dependent Raman spectra are shown that identify electrodeposition conditions where Ge films can be deposited with either long- or short-range crystalline order. Raman spectra collected with electrodeposited Ge films immersed in solutions containing CN$^-$(aq) did not indicate a significant presence of pinholes that exposed the underlying Au(s) substrate. Raman spectra were also collected that identified a potential-dependence for Ge hydride formation at the interface of these films. Separate spectra were collected for the oxidative dissolution of Ge in solution and the complete dry oxidation of Ge to GeO$_x$ in air. These data sets cumulatively represent the first demonstration of the overlayer SERS strategy to follow surface chemical processes at crystalline, nanostructured, Ge materials *in situ* and in real time.

KEYWORDS: Raman · SERS · germanium · electrodeposition · surface chemistry
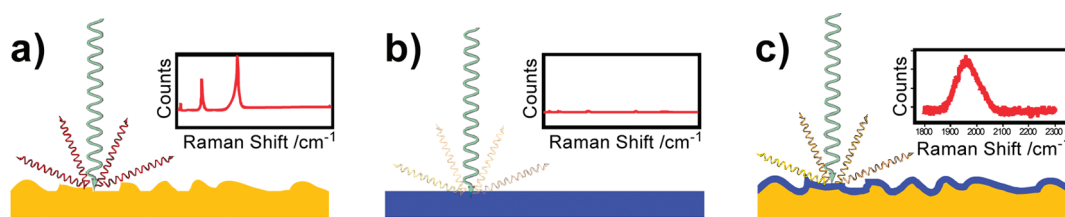
Figure 1. Idealized depiction of overlayer SERS enhancement induced by an active substrate. (a) SERS active, nanostructured substrate. (b) Non-SERS active semiconductor showing weak/no Raman signatures for surface groups and chemisorbates. (c) Raman spectra obtained on a conformal, pinhole-free semiconductor film on top of a SERS active substrate.

powerful electroanalytical tool for elucidating vibronic information in media of interest at low frequencies.[11−14] However, despite routine use of Raman microscopy in the semiconductor industry to monitor bulk semiconductor properties/defects during processing,[15] comparatively few studies have utilized the SERS effect to study the structural and chemical properties of semiconductor surfaces.

The first reports of surface-enhanced Raman spectra of semiconductor surfaces involved cast or electrodeposited films of SERS-active metal colloids on planar semiconductor substrates.[16,17] Although this approach is general to all interfaces, the method suffers from an ill-defined, uneven enhancement of molecular vibrations near "hot-spots" that are not necessarily limited to only the vibronic processes at the semiconductor interface of interest. Two improvements to this original concept have been developed. The first variation uses the metal tip of a scanning probe system as the source of the SERS enhancement (tip enhanced Raman spectroscopy (TERS)).[18] Although rich spectroscopic measurements correlated with topographical features have been demonstrated using TERS, the experimental demands for aligned and optimized optics/electronics, the premium for highly engineered tips, the incompatibility with caustic environments, and the general difficulty encountered with scanning probe studies in liquid media limit the types of surface analyses that can be routinely performed. The second variation involves SERS-active colloids that are coated with a thin, insulating, and chemically inert layer (shell-isolated nanoparticle-enhanced Raman spectroscopy-SHINERS).[19] This strategy is ill-suited for *in situ* study of semiconductor interfaces in reactive media. Coating an interface with a film of blocking, SERS-active colloids artificially perturbs mass transport of chemical reactants to the surface and intractably complicates rate measurements of surface reactions and surface coverage homogeneity. Resonantly enhanced Raman signatures have also been explored.[20] For thin semiconductor films, excitation with supra-bandgap light resonantly enhances the bulk phonon modes of the semiconductor lattice.[20] This approach provides no direct insight on surface chemistry and also increases the possibility of deleterious photo(electro)chemical processes that could degrade the semiconductor

material. Resonant enhancements can also strongly increase (10^3-10^4) the signals specifically for vibronic features of conjugated adsorbates at the surface of semiconductor nanoparticles.[21−31] A recent report utilizing ultrapure semiconductor quantum dots prepared *via* molecular beam epitaxy suggests such resonant enhancements can approach the levels typically observed for colloidal metal SERS substrates.[32] However, the generality and precise source of this magnitude of signal enhancement and the extent that the resonance perturbs the nature of surface−adsorbate bonding have yet to be determined.

The overlayer SERS approach[33,34] is an alternative, under-utilized strategy for investigating the structure and surface bonding of non-SERS-active semiconductors. This strategy has been used extensively to study the deposition and adsorbate chemistry of non-SERS active transition metals[35−37] and insulators.[38,39] In this scheme, a SERS-active metal substrate is coated with a conformal thin film of the non-SERS active material of interest (Figure 1). When the film thickness is kept ultrathin (≤5 nm), the SERS-effect from the underlying support substrate extends through the overlayer and significantly enhances the phonon and adsorbate vibrational modes at the top interface that are otherwise too weak to detect.[35,40] Despite the success of this strategy in the study of catalytic and insulating dielectric materials, to date, it has not yet been exploited to study either the deposition process for, or the interfacial chemical reactions of, nanostructured Ge materials in detail.

The goals of this initial work are 2-fold. The presented electrochemical and spectroscopic data illustrate the utility of this SERS approach for monitoring, deconvoluting, and understanding the electrodeposition process of ultrathin Ge films at a nanostructured, polycrystalline Au interface. The data demonstrate that under controlled electrodeposition conditions, conformal and pinhole-free Ge films are readily prepared on these substrates and that the SERS effect enables facile detection at the single monolayer level. Separately, the data herein also show that the overlayer SERS scheme can be leveraged to study the chemistry of crystalline Ge interfaces directly in both liquid and air ambient and in real-time. Time-dependent spectra are presented that describe Ge dissolution in solution,
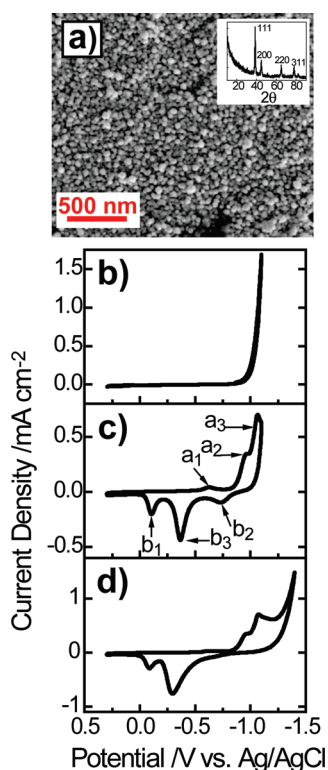
Figure 2. (a) Scanning electron micrograph of a top-down view of a SERS-active Au nanoparticle film. Inset: X-ray diffraction pattern of film showing characteristic signatures for polycrystalline Au. (b−d) Voltammetric responses for Au nanoparticle film electrodes immersed in (b) deaerated buffered solution (pH = 9.3) containing 0.010 M $Na_2B_4O_7$ and 0.5 M Na_2SO_4 and (c) after addition of 0.001 M GeO_2 in the same electrolyte. (d) Same as in panel c but with a vertex potential of −1.4 V vs Ag/AgCl. Scan rate = 0.01 V s^{-1}.

potential-dependent surface hydride formation, and oxidation. Opportunities for utilizing this scheme to study aspects of the electrodeposition and surface reactivity of Ge in ways that are inaccessible by any other analytical methodology are discussed.

RESULTS

Au Nanoparticle Film Electrodes. Figure 2a shows an electron micrograph of a Au nanoparticle film electrode after plating excess Au to increase the diameters of the nanoparticles. After this treatment, the Au nanoparticles uniformly possessed a mean diameter of ∼50 nm. The inset of Figure 2a shows a thin-film X-ray diffraction pattern for the Au nanoparticle films after "ripening'" with $HAuCl_4$(aq). Spectral features for (111), (200), (220), and (311) surface planes were observed, consistent with a face-centered-cubic, polycrystalline Au interface. The ratio, γ, between the projected geometric area and the true electrochemically active surface area for these Au nanoparticle film electrodes was determined from the integrated charge measured during the underpotential deposition of Cu from aqueous solution (Supporting Information). From these data, a nominal surface roughness factor of ∼7

was consistently observed for the Au nanoparticle film electrodes. The SERS activity of these Au nanoparticle films was assessed by comparing the intensity for spectra of pyridine dissolved in solution as compared to adsorbed at the surface, normalizing for the relative number of molecules probed in each measurement.[41] Films prepared in this manner consistently gave a SERS amplification of $>10^5$ for excitation at λ = 632.8 nm across the entire electrode surface (Supporting Information).

Ge Electrodeposition at Au Nanoparticle Film Electrodes. Representative voltammetric responses (normalized to the projected geometric electrode area) for the Au nanoparticle films in aqueous solution at pH = 9.3 are shown in Figures 2b−d. In buffered electrolyte, no faradaic processes were noted between +0.3 to −0.9 V vs Ag/AgCl. The onset for H_2 evolution was observed at ca. −0.95 V vs Ag/AgCl. Addition of 0.001 M GeO_2 to solution introduced new features in the current−potential response. At this pH, the expected standard potential for the GeO_2/Ge redox couple is −0.98 V vs Ag/AgCl.[42] As shown in Figure 2b, three reductive (a_1-a_3) and oxidative (b_1-b_3) features were evident in this solution. A series of cyclic voltammograms were performed with switching potentials between −0.7 and −1.1 V vs Ag/AgCl (Supporting Information) to identify the correlation between the reductive and oxidative features. The onset for the first cathodic wave, a_1, was at −0.55 V vs Ag/AgCl and was associated with the anodic wave, b_1, centered at −0.1 V vs Ag/AgCl. The integrated charges for these two waves were independent of scan rate, consistent with an adsorptive deposition process. The second and third cathodic waves were not well separated. The cathodic wave, a_2, was centered at −0.95 V vs Ag/AgCl and gave rise to the anodic wave, b_2, beginning at −0.85 and centered at −0.75 V vs Ag/AgCl. The charges associated with these features were partially sensitive to the total time the electrode was poised at potentials more negative than −0.95 V vs Ag/AgCl. The third cathodic signal, a_3, overlapped significantly with a_2 and was centered at −1.07 V vs Ag/AgCl. The anodic wave, b_3, centered at −0.35 V vs Ag/AgCl was associated with a_3. The integrated charges for these voltammetric features were strongly affected by the total time the electrode was poised at potentials more negative than −1.0 V vs Ag/AgCl, with the total stripping charge for feature b_3 increasing progressively at longer times (Supporting Information). The cathodic process a_3 was not related to H_2 evolution, which was shifted to more negative potentials by ∼0.3 V (Figure 2d). The features for aqueous Ge electrodeposition observed here for these nanostructured, polycrystalline Au interfaces closely follow those recently reported for flat, single-crystalline Au(111) electrodes.[43]

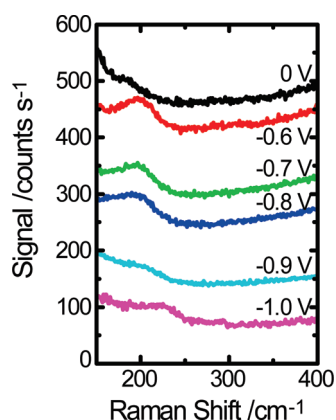**Raman Analyses During Ge Electrodeposition.** Raman spectra between 125 and 400 cm^{-1} were obtained

Figure 3. Raman spectra recorded at Au nanoparticle film electrodes immersed in a buffered aqueous solution at pH = 9.3 containing 0.010 M $Na_2B_4O_7$, 0.001 M GeO_2, and 0.5 M Na_2SO_4. Spectra were obtained using λ = 632.8 nm at 3.9 mW and with the electrode biased at the indicated potential. For potentials between 0 and −0.9 V *vs* Ag/AgCl, the electrode was poised for 180 s prior to spectral acquisition. At −1.0 V *vs* Ag/AgCl, the spectrum was obtained after 10 s. The spectra are not intentionally offset, and differences in the vertical height represent changes in the total background counts at more negative potentials.
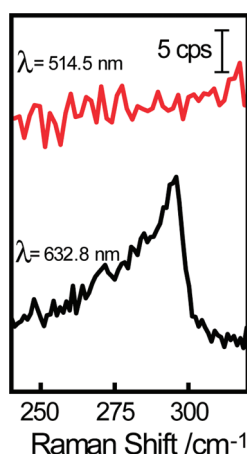

Figure 4. Raman spectra recorded at a Au nanoparticle electrode using either 632.8 (3.9 mW) or 514.5 nm (4.9 mW) excitation after Ge electrodeposition at −1.0 V *vs* Ag/AgCl for 120 s in the same electrolyte as Figure 2. Spectra are offset for clarity.

with Au nanoparticle film electrodes poised at several potentials while immersed in alkaline GeO_2-containing solutions and are shown in Figure 3. Spectra taken with the electrode poised at 0 V *vs* Ag/AgCl were featureless and identical to spectra recorded either with the dry electrodes before immersion or with the electrodes immersed in blank electrolyte. Spectra obtained at potentials between 0 and −0.5 V *vs* Ag/AgCl were unchanged. The Raman spectra collected when the electrode was biased at −0.6 V *vs* Ag/AgCl were distinct in two aspects. First, the total recorded counts across the entire interrogated range decreased in a consistent fashion across seven separately tested electrodes. Second, a new, broad signature centered at 200 cm^{-1} was evident. Neither change was observed in the absence of dissolved GeO_2. These two spectral features could also be reversibly removed by returning the electrode to 0.0 V *vs* Ag/AgCl, indicating that the spectral changes were associated with the adsorption of a reduced Ge-containing species, that is, the cathodic process a_1 in Figure 2c. At progressively more negative potentials, the total recorded counts continued to decrease. At −0.9 V *vs* Ag/AgCl, the feature at 200 cm^{-1} disappeared. Throughout this entire range of potentials, these spectral features were not time-sensitive.

Polarization of the electrodes at −1.0 V *vs* Ag/AgCl resulted in Raman spectra that changed significantly with time. The spectrum in Figure 3 for the electrode at −1.0 V *vs* Ag/AgCl was recorded 10 s after initial polarization. The aforementioned signature near 200 cm^{-1} was not observed, and the spectral region between 250 and 300 cm^{-1} was empty. Figure 4 shows the Raman spectra for the same electrode after 120 s of

polarization time. Using "short" wavelength excitation (514.5 nm), no spectral features were observed even at these longer times. However, a strong signature near 300 cm^{-1} was consistently observed when longer wavelength excitation was used. This feature in Figure 4 corresponds to the bulk phonon mode for crystalline Ge exhibiting quantum confinement.[44,45] The observation of this Ge phonon mode only with longer wavelength excitation is consistent with the premise that the SERS activity of the underlying Au substrate specifically makes detection possible.[36] Figure 5 shows the intensity and peak position of this Ge phonon mode as a function of polarization time. At polarization times less than 60 s, the Ge phonon mode could not be accurately resolved above the background. At longer polarization times, the full width at half-maximum (fwhm) of the Ge phonon mode decreased slightly and its position was blue-shifted from 291.1 ± 0.6 cm^{-1} to 297.2 ± 0.4 cm^{-1} (Figure 5b,c). The greatest change in these two parameters occurred at short times. After this initial period, these features remained constant and never reached values equivalent to those recorded for a bulk single-crystal Ge sample, consistent with crystalline Ge that retains physical dimensions shorter than the Bohr exciton radius. Relative to the spectrum for bulk Ge(111), the phonon mode from the electrodeposited Ge film was less intense, more broad, and centered at a lower frequency than the phonon mode for the Ge(111) sample at all investigated electrodeposition times. The integrated peak intensity for the Ge phonon mode increased with longer electrodeposition times but exhibited a decidedly nonlinear time-dependence (Figure 5d). The time-dependent profile of the stripping charge density for anodic feature b_3 was separately recorded and is shown in Figure 5e. When plotted as a function of the corresponding stripping charge density (voltammetric feature b_3 in Figure 2c),
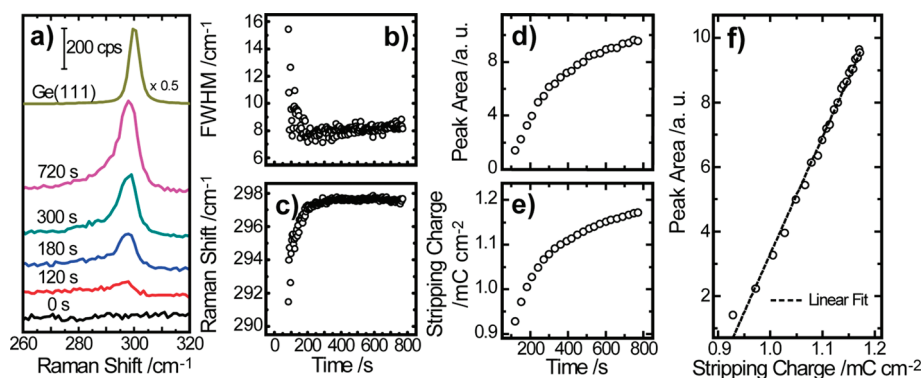
Figure 5. (a) Time dependent Raman spectra acquired during polarization at −1.0 V *vs* Ag/AgCl of a Au nanoparticle film electrode immersed in a buffered solution (pH = 9.3) containing 0.001 M GeO$_2$, 0.010 M Na$_2$B$_4$O$_7$, and 0.5 M Na$_2$SO$_4$. Integration time = 3 s. (b) Full-width at half-maximum, fwhm, as a function of polarization time. (c) Peak position of Ge phonon mode as a function of polarization time. (d) Integrated area of Ge phonon mode recorded after electrodeposition at −1.0 V *vs* Ag/AgCl as a function of electrodeposition time. (e) Stripping charge density of anodic wave b_3 as in Figure 2 after biasing Au nanoparticle electrode at −1.0 V *vs* Ag/AgCl as a function of electrodeposition time. (f) Integrated area of the time-dependent Ge phonon intensity as a function of stripping charge density of anodic feature b_3 at the corresponding electrodeposition time.

the integrated peak intensity for the Ge phonon was strongly and linearly correlated with the amount of "bulk" Ge electrodeposited onto the surface (Figure 5f). These data also show that the onset of the Ge phonon mode occurred at electrodeposition charge densities ≥ 0.8 mC cm^{-2}, the approximate charge density needed to deposit a complete monolayer of Ge through a 4e^{-} process (assuming a monolayer density of 1.5×10^{15} atoms cm^{-2}).[43] From the data in Figure 5a,f, an enhancement factor of 4×10^4 was determined for the electrodeposited Ge films (Supporting Information).

Repetition of these experiments at more negative electrodeposition potentials resulted in Ge films with decidedly different spectral features. Figure 6 illustrates the difference in the Ge phonon mode seen at various deposition potentials. At −1.0 or −1.1 V *vs* Ag/AgCl, the Raman spectra for the electrodeposited Ge films showed a strong, sharp signature as in Figures 4 and 5. At more negative potentials, the intensity of the phonon mode significantly decreased, and the peak position was red-shifted to *ca.* 290 cm^{-1}. An irreversible change between the spectra collected at −1.1 V and −1.2 V for electrodeposited Ge films initially showing Raman spectra with a strong, sharp phonon mode at 297 cm^{-1} was similarly observed (Supporting Information). The attenuated phonon mode intensity and peak shift was not correlated with a mechanical loss of Ge in contact with the Au nanoparticle film electrode. Separate stripping voltammograms indicated that the integrated charge for the anodic peak at −0.3 V *vs* Ag/AgCl (*i.e.*, feature b_3 in Figure 2c) did not statistically decrease when the electrode was biased more negative than −1.1 V *vs* Ag/AgCl. The spectral features in Figure 6 are consistent with Ge surface phonon modes, which correspond to localized, short-range Ge lattice vibrations.[46] The spectra suggest that
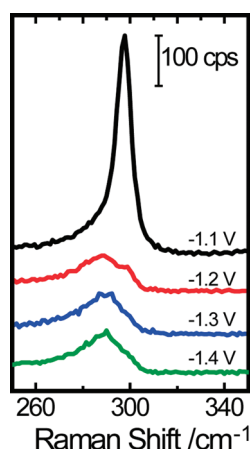

Figure 6. Raman spectra acquired after poising an electrodeposited Ge film at more negative potentials in the same electrolyte as in Figure 2.

long-range order and crystallinity is compromised when the electrodeposited Ge films are biased at more negative potentials, but the film apparently does not become fully amorphous, since a Raman band near 270 cm^{-1} for amorphous Ge was never observed.[47−49] The lack of any amorphous Raman signatures in Figure 6 suggests that the Ge films retain some local, short-range degree of crystallinity. *Ex situ* collection of thin film X-ray diffraction patterns was attempted to assess the crystallinity of the electrodeposited Ge, but the difficulty in getting spectra with sufficient signal-to-noise for these films prevented a separate validation of this hypothesis.

Raman Spectra Recorded During Anodic Decomposition of Ge Films. The dissolution of the electrodeposited Ge films in the same electrolyte could also be followed by Raman spectroscopy. Figure 7a shows the time-dependent Raman spectra for a Ge film electrode (electrodeposited at −1.0 V *vs* Ag/AgCl for 14 min) that was
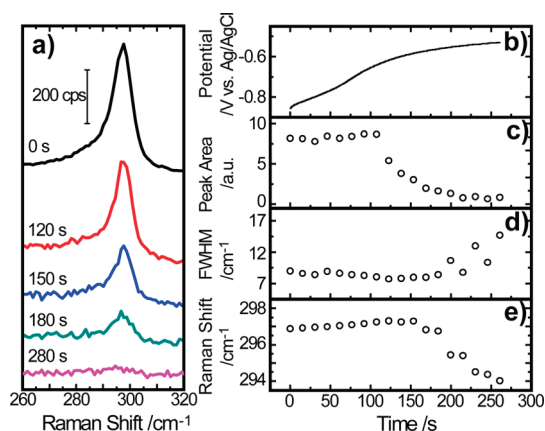
Figure 7. (a) Time-dependent Raman spectra for electrodeposited Ge films acquired at open circuit after cathodic polarization at −1.0 V *vs* Ag/AgCl. Integration time = 10 s. (b) Potential of electrode during oxidation/dissolution at open circuit, (c) integrated area, (d) full-width at half-maximum, fwhm, and (e) peak center of Ge phonon mode as a function of time.

left at open-circuit. Figure 7b shows the recorded potential of the Ge film electrode, with the electrode drifting to more positive potentials at longer times. As long as the electrode potential was more negative than −0.7 V *vs* Ag/AgCl, there were no observable changes in the Ge phonon spectra. However, as the electrode potential approached −0.6 V *vs* Ag/AgCl (where the anodic process b_3 began in Figure 2c) the intensity of the Ge phonon mode decreased (Figure 7a,c) but without a substantive change in the fwhm and peak position (Figure 7d,e). The values of the peak position and fwhm only changed at longer times, in accord with the dissolution of ultrathin Ge films.

Defect Monitoring in Electrodeposited Ge Films. The integrity and extent of film uniformity across the surface of the Au nanoparticle electrodes were assessed with an adsorptive molecular probe. CN⁻(aq) binds strongly to metallic Au(s) and demonstrates intense and unique Raman signatures when adsorbed at a Au(s) interface and is thus a powerful probe for identifying overlayer film defects (Figure 8a).[50−52] Potential-dependent Raman spectra were collected in blank electrolyte with 0.001 M KCN between 0 V and −1.1 V. The C≡N stretching mode of CN⁻ adsorbed onto Au(s) was clearly visible at 2110 cm⁻¹ (Figure 8b). Analogous spectra obtained at different applied biases showed the characteristic Stark shift of adsorbed CN⁻ to lower frequencies at more negative potentials (Supporting Information).[14,50] In a separate experiment, the Au nanoparticle film electrode was immersed in the buffered solution with dissolved GeO₂ and poised at −0.8 V *vs* Ag/AgCl while another Raman spectrum was obtained (Figure 7c). A spectral signature for adsorbed CN⁻ was still clearly observable, but the integrated intensity was decreased to 45% of the intensity at the pristine Au(s) interface. These data suggest that at these conditions the Au electrode surface becomes partially
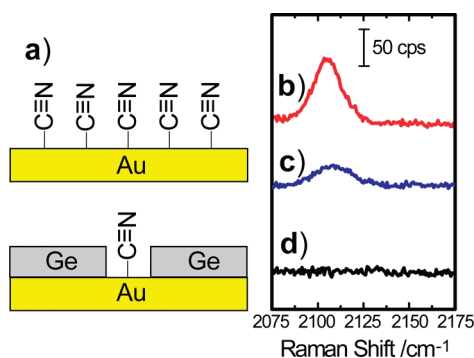

Figure 8. (a) Depiction of "end-on" CN⁻ adsorption at (top) a bare Au electrode and at (bottom) pinholes on a Ge-coated Au electrode. (b) Raman spectra for a Au nanoparticle film electrode immersed in a deaerated solution containing 0.01 M Na₂B₄O₇, 0.5 M Na₂SO₄, and 0.001 M KCN and poised at −0.8 V *vs* Ag/AgCl. (c) Raman spectra for a Au nanoparticle film electrode after the addition of 0.001 M KCN to a solution containing 0.01 M Na₂B₄O₇, 0.001 M GeO₂, and 0.5 M Na₂SO₄. The electrode was poised at −1.0 V *vs* Ag/AgCl for 120 s before addition of KCN and then at −0.8 V to prevent additional deposition while preserving the film. (d) Raman spectra for a Au nanoparticle film electrode after the addition of 0.001 M KCN to a solution containing 0.01 M Na₂B₄O₇, 0.001 M GeO₂, and 0.5 M Na₂SO₄. The electrode was poised at −1.0 V *vs* Ag/AgCl for 120 s before addition of KCN.

covered with adsorbed Ge species which do not bind with CN⁻ and are not displaced by CN⁻ adsorption on Au(s). A related experiment was then performed by first polarizing the electrode at −1.0 V for 120 s in the buffered electrolyte to deposit a Ge monolayer film that exhibited the characteristic Ge phonon mode. The electrode potential was then lowered to −0.8 V to stop additional deposition while protecting the film from dissolution. KCN was added to effect a 0.001 M CN⁻ concentration, and a Raman spectrum was then obtained (Figure 8d). Under these conditions no signal indicative of CN⁻ adsorbed to Au(s) was evident, indicating that electrodeposition of Ge by this method produced uniform films devoid of pinhole defects accessible by this adsorptive molecular probe.

Ge Surface Chemistry: Ge−H$_x$. Previous investigations of crystalline Ge electrode interfaces have shown that surface hydride formation in aqueous solutions can be controlled by an applied potential.[53] To determine whether electrodeposited Ge films demonstrated interfacial chemistry akin to a bulk, single-crystalline Ge electrode, the Raman signals between 1800 and 2200 cm⁻¹ were recorded as a function of applied bias after immersing the electrodeposited Ge films into a blank, buffered, and deaerated electrolyte. In this spectral region, the stretching modes for surficial Ge−H$_x$ (where x = 1−3) moieties are Raman-active (Figure 9).[54,55] In Figure 9a, the Ge film electrode was initially poised at −0.8 V *vs* Ag/AgCl. At both −0.8 and −0.9 V *vs* Ag/AgCl, no spectral signatures indicative of surficial Ge−H$_x$ stretches were observed above the baseline. At −1.0 V *vs* Ag/AgCl, a broad signal centered
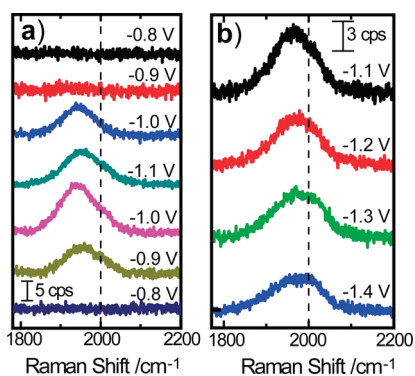
Figure 9. Potential-dependent Raman spectra showing Ge−H$_x$ modes at electrodeposited Ge films. (a) The film was first prepared at −1.1 V *vs* Ag/AgCl for 10 min, then rinsed, dried, and transferred to an aqueous solution containing 0.01 M Na$_2$B$_4$O$_7$ and 0.5 M Na$_2$SO$_4$. Spectra were acquired sequentially (top to bottom) at −0.8, −0.9, −1.0, −1.1, −1.0, −0.9, and −0.8 V *vs* Ag/AgCl. (b) A separate electrode prepared as in panel A was biased for 120 s at each indicated potential.

at 1945 cm^{-1} was detected. The position of this symmetric signature was broadly consistent with a predominance of Ge monohydride (Ge−H) at the surface of the electrode.[56,57] When the electrode was biased more negatively at −1.1 V *vs* Ag/AgCl, the position of the observed Raman signature blue-shifted slightly to 1951 cm^{-1}, the total intensity increased, and the spectral shape became more asymmetric (with an additional sideband at larger Raman shifts). The increased signal at >2000 cm^{-1} is consistent with the formation of additional dihydride (Ge−H$_2$) surface moieties.[57] When the electrode was stepped back to −1.0 V *vs* Ag/AgCl, the spectral shape red-shifted back to 1941 cm^{-1}, the total intensity continued to increase, and the sideband at larger Raman shifts was still evident. After the electrode was then stepped back down to −0.9 V *vs* Ag/AgCl, the signal for Ge hydride stretches was still observable, in contrast to the previous spectrum collected at this same potential. The total integrated intensity of the Ge hydride response was smaller than in the prior spectrum obtained at −1.0 V *vs* Ag/AgCl. When the electrode was biased at −0.8 V *vs* Ag/AgCl, no signatures for Ge hydride surface moieties were noted. A separate set of spectra was also acquired, where the electrode was biased to potentials where the main phonon mode disappeared as in Figure 6 (Figure 9b). In these spectra, the intensity of the shoulder at Raman shifts larger than 2000 cm^{-1} increased and became the more pronounced feature, indicating a greater extent of Ge−H$_2$ bonding throughout the electrodeposited film.

Ge Surface Chemistry: Surface Oxidation. Time-dependent Raman spectra were acquired with a freshly electrodeposited, crystalline Ge film exposed to air in order to determine if the rate and extent of oxidation could be followed by Raman measurements. After emersion from the GeO$_2$-containing electrolyte, the
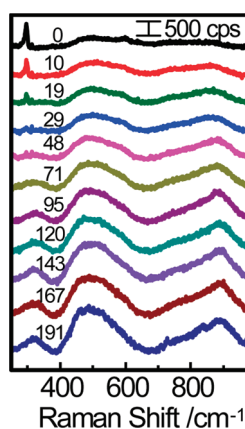

Figure 10. Raman spectra of a Ge film electrodeposited at −1.1 V *vs* Ag/AgCl after emersion, rinse, and drying in a stream of N$_2$(g). The numbers correspond to the time exposed to dry ambient lab air in minutes.

Ge film was rinsed and dried under a stream of N$_2$(g) gas. Raman spectra of the dried electrodeposited Ge film were then collected as a function of time after direct exposure to ambient air. Figure 10 highlights the time profile for a dry ultrathin Ge film under these conditions. Initially, the Ge phonon mode near 300 cm^{-1} was the only strong, identifiable spectral feature. During continued exposure to the lab ambient, the crystalline Ge phonon mode decreased in intensity on the time scale of minutes. After 29 min of exposure to air, the Raman spectral feature for crystalline Ge was no longer observable. In contrast to the dissolution spectra in Figure 7, spectral features between 400 and 975 cm^{-1} appeared concomitantly and became increasingly more pronounced at longer times. The broad spectral feature between 400 and 650 cm^{-1} is commensurate with the Raman signature for vitreous GeO$_x$, specifically Ge−O−Ge stretching and breathing modes.[58−63] The features centered near 320 and 875 cm^{-1} are consistent with both Raman and infrared modes of phonon modes in glassy GeO$_x$.[64,65] The relative intensity of these modes, which are typically much weaker in the Raman spectra for bulk vitreous GeO$_x$, demonstrate the relaxation of the selection rules for purely Raman- and IR-active modes in the obtained SERS spectra.[66−68] The spectra in Figure 10 illustrate that the films exhibit meta-stability under ambient conditions and that their oxidation product is a disordered, glassy oxide.

DISCUSSION

Raman Analyses During Electrodeposition. The presented data collectively highlight the ability of the overlayer SERS approach to give insight on the deposition of ultrathin films of semiconductor materials in real time. Raman spectra could not be obtained during the initial stages of Ge electrodeposition without the SERS-effect from the underlying Au substrate. The indirect bandgap of Ge substantially weakens the

resonant Raman signal enhancement (relative to semiconductors like CdS or InAs)[69,70] with the excitation wavelengths used here. The SERS-enhancement observed here afforded the opportunity to study the Ge electrodeposition process and the resultant properties of the electrodeposited semiconductor films in detail. Specifically, *in situ* information on the amount deposited, order/crystallinity, uniformity of surface coverage, and stability of the Ge films were readily interpreted from the collected spectra. Although similar information could also have been obtained separately with scanning probe and quartz crystal microbalance measurements, these techniques are not fast, high-throughput analyses methods and are not easily applied to nonplanar, nanostructured interfaces. Prior to this work, only Ge electrodeposition processes at planar, single-crystalline interface had been described, and it was not known to what extent Ge electrodeposition processes on textured, polycrystalline, and nanostructured interfaces differed. The present data indicate that ultrathin Ge films electrodeposited on a packed Au nanoparticle film can exhibit a high degree of crystallinity and uniformity under specific electrodeposition conditions, a surprising and unusual feature for electrodeposition of group IV semiconductors.[71,72]

The monotonic relation between the relative intensity of the crystalline Ge phonon mode and the total amount of Ge electrodeposited onto the electrode support indicated this Raman signature is a useful gauge of the thickness of the deposited Ge film in real time. Further, the extreme sensitivity of the spectral features of phonon modes (*i.e.*, peak position and shape)[73,74] toward morphology in semiconductor films with effective thicknesses less than the Bohr exciton radius[75] provided an additional means to prepare precisely Ge thin films in the quantum confinement size-regime. In conjunction, the potential-dependence of the Ge phonon mode marked conditions that either preserve or destroy the long-range crystallinity and order in the electrodeposited Ge films without inducing a conversion to an amorphous, glassy film. This level of control is particularly useful in the design of thin Ge films for optoelectronic applications, where nanocrystalline Ge has distinct photoluminescent properties. A comparison of the optoelectronic properties of Ge with varied and controlled degrees of crystallinity would be useful and should be possible *via* electrochemical preparation.

Despite the macroscale ($\sim$10 μm^2) spot size used to collect Raman spectra in this work, the use of a molecular probe adsorbate verified the absence of microscopic defects in the as-deposited films and validated the model of a conformal, pinhole-free Ge film produced *via* the employed electrodeposition parameters. The macroscale integrity of electrodeposited, monolayer-thick Ge films is somewhat surprising

as the SERS-active Au support electrodes are neither single-crystalline nor rigorously flat and the bulk deposition of Ge is not itself a self-limiting, underpotential electrodeposition process. Although an underpotential electrodeposition of a submonolayer of Ge was noted separately in the electrochemical and Raman data, this layer did not completely and uniformly coat the underlying Au electrode surface. The clear Raman signals for CN$^-$ adsorbed onto exposed Au(s) observed in solutions containing KCN suggest that $\sim$45% of the underlying Au surface is left exposed after the underpotential deposition of Ge. Accordingly, electrodeposition of Ge at overpotentials should proceed by a discrete nucleation (*i.e.*, Volmer–Weber film growth), as is commonly observed in metal electrodeposition processes.[76] Separate analyses of the current density-time transients for Ge electrodeposition at overpotential conditions could not be fit using the models developed for electrodeposition *via* a Volmer–Weber process (Supporting Information),[77] suggesting the growth of the Ge films proceeded by an alternative mechanism involving uniform electrodeposition. The lack of Raman signatures for CN$^-$ adsorbed on Au(s) corroborate this hypothesis, indicating that even a monolayer thick Ge film produced *via* electrodeposition at overpotentials at Au surfaces are uniform and complete. These data are consistent with the possibility that the initial submonolayer of Ge may specifically template the deposition of pinhole-free and crystalline "bulk" Ge films. Separate Raman measurements using electrode surfaces that favor or inhibit the electrodeposition of a submonolayer of Ge at underpotential conditions are currently ongoing to determine whether this feature systematically influences the "bulk" electrodeposition of Ge. Such information would be useful to better understand conditions that favor the electrochemical preparation of high-quality Ge and related group IV semiconductor films.

***In Situ* Raman Analyses of Ge Surface Chemistry.** The presented data highlight a unique advantage afforded by the demonstrated platform for the study of bonding at Ge surfaces, that is, the ability to measure both low and high frequency vibrations. The spectra collected separately for the H-termination and the oxidation of Ge interfaces demonstrate this aspect as well as the ability to quickly and readily measure surface chemical processes with good signal-to-noise both in liquid (with or without potential control) and air ambients. This work elucidated two interesting features regarding surface hydride formation in ultrathin Ge films. First, the changes in the spectra shown in Figure 8 were consistent with a quasi-reversible, potential-dependent Ge hydride formation and agree well with the voltammetry in Figure 2c. Previous reflectance-based IR studies by Chazalveil and co-workers[53,57] and electrochemical measurements by Gerischer and co-workers[78] have detailed potential-dependent Ge–H$_x$

formation at single-crystalline Ge(111) and Ge(100) electrode interfaces. Using reflectance angle infrared spectroscopy, Chazalveil and co-workers surmised that atop Ge atoms were hydroxyl-terminated at positive potentials and then became hydride-terminated at potentials close to the reduction potential of H^+. The background signal for dissolved OH^- at higher Raman shifts in the system studied here precluded unambiguous determination of surface hydroxyl groups. Nevertheless, the Raman spectra in Figure 8 of this work are in strong agreement with the potential dependence of surface H-termination. These data suggest that the behavior of the surfaces of the Ge films electrodeposited between −1.0 and −1.1 V *vs* Ag/AgCl closely follows the behavior observed at ordered, single crystalline Ge interfaces. Simply, the chemical processes at these electrodeposited Ge films mirror those at "bulk" Ge interfaces and thus are viable platforms for studying chemical reactions and bonding at crystalline Ge interfaces. Surface Ge−H bonds have been used as chemical handles for the wet chemical formation of surficial Ge−C bonds through hydrogermylation of alkenes and alkynes.[79] Ge−H bonds have also been used to prepare surficial Ge-X (where X = Cl or Br) groups, which can then be subsequently reacted with alkylating or thiol reagents to effect Ge−C or Ge−S bonding, respectively.[80−82] Despite the extensive *ex situ* characterization of these Ge surface functionalization strategies, there are no *in situ* studies of surface bond formation. Such studies would provide a means to elucidate reaction mechanisms and factors that influence desirable and deleterious reaction pathways.

The second interesting feature in these Raman spectra is the correlation between the loss of the crystalline phonon mode and the increase in signatures for $Ge-H_x$ ($x > 1$) at more negative potentials ($< −1.1$ V *vs* Ag/AgCl). Increased structural disorder in bulk, single-crystalline Ge electrode interfaces immersed in aqueous solutions at strongly negative potentials has been observed by several groups through scanning probe microscopies.[43,83,84] The data shown here corroborate these prior observations but directly implicate the increased hydrogenation of Ge atoms as the specific cause of lattice disruption in these electrodeposited thin films. This structural disorder induced by excessive hydrogenation of Ge atoms in the film could not be simply reversed by reapplication of less negative potentials, that is, a recovery of the phonon mode intensity was never observed (Supporting Information). This feature stands in contrast to the reversible order−disorder transition observed in scanning tunneling microscopy measurements of single-crystalline Ge electrode interfaces biased at positive and negative potentials.[83,84] Apparently, once a critical amount of disorder is induced in the electrodeposited Ge films described here, there is

no simple potential-dependent mechanism to restore long-range order.

The presented Raman data also show that both the rates for and the types of surface chemical processes at these Ge films can be studied in detail. The rapid oxidation and dissolution of Ge in air and solution, respectively, is not surprising, per se. However, kinetic measurements of these processes are not easily obtained using standard methods. Such information could be used to understand the chemical factors that influence degradation processes. For example, *ex situ* data highlighting the differences in the type of oxide formed at either H-terminated or Cl-terminated Ge surfaces have been reported.[85] Empirical measurements following oxide growth indicate that a hydrated and disordered (GeO_x) oxide is formed on H-terminated Ge while a more ordered, stoichiometric (GeO_2) oxide is formed on Cl-terminated Ge surfaces. No experimental data highlighting mechanistic information for these differences have thus far been collected but the methodology shown here suggests such information is attainable. Similarly, the resistance against oxidation that alkyl- and thiol-based passivation layers impart on Ge interfaces has only been indirectly assessed. For the improvement and further design of chemical passivation layers, a molecular-level understanding of their failure mechanisms is needed. Separately, the chemistries of GeO_2 (or GeO_x) interfaces are also interesting in their own right. Recent reports have separately demonstrated new chemical pathways to form reduced Ge−C bonds at low temperatures at GeO_2 using base-catalyzed reactions with alkylcarbonates[86] and thiol-based reactions to form stable Ge−S bonds at elevated temperatures.[87] These unexpected and potentially useful reaction processes are intrinsically complex multistep heterogeneous reactions and are not understood. SERS-derived spectra of GeO_2 films, during the course of such a reaction may shed light on the possible reaction mechanisms. Given the known parallels between the chemistry of Ge and Si,[88] a better understanding of the reactivity of oxidized Ge surfaces may also provide chemical insight on how to activate and reduce SiO_2 interfaces, a chemical process with significant fundamental and practical value.[89]

CONCLUSION

The SERS activity of close-packed, Au nanoparticle film electrodes was used to study the initial details of Ge electrodeposition from aqueous solution. The recorded electrochemical and Raman spectra indicated that a submonolayer of Ge initially deposits at underpotential deposition conditions and that "bulk" crystalline Ge deposits at low overpotential conditions. Under the investigated parameters, the deposition rate of crystalline Ge is slow enough that Raman spectra can be used to identify conditions that allow the preparation of films exhibiting quantum confinement effects.

Separate Raman spectra demonstrated that the as-deposited films did not possess a detectable level of pinhole defects. Raman spectra also indicated that at high overpotential conditions, the resultant Ge film is significantly less crystalline. Examination of the spectral region corresponding to Ge—H_x modes indicated that the as-deposited films become H-terminated at applied potentials more negative than −1.1 V *vs* Ag/AgCl at pH = 9.3. The Raman spectra for Ge films at large overpotentials exhibit signatures indicative of Ge atoms coordinated with more than one —H group, in accord with the increased disorder implied by the recorded phonon mode. For Ge films exhibiting a predominance of only Ge—H surface moieties, the Raman data indicated that the surface atoms could be reversibly H-terminated as a function of applied potential. Separate time-dependent Raman spectra of electrodeposited crystalline Ge films showed that oxidative processes could be followed *in situ* and in real time. These data highlight the capacity of this strategy for studying surface chemical processes of crystalline Ge interfaces with heretofore unattainable temporal and spectroscopic detail.

METHODS

Materials and Chemicals. Methanol (Certified ACS, Fisher), acetone (Certified ACS, Fisher), isopropyl alcohol (Certified ACS, Fisher), $H_2N(CH_2)_3Si(OC_2H_5)_3$ (99%, Aldrich), $HAuCl_4 \cdot H_2O$ (99.9%, Strem Chemicals), $Na_3C_6H_5O_7$ (98%, Acros Organics), NH_4OH (50 wt % in H_2O, Aldrich), GeO_2 (99.98%, Alfa Aesar), Na_2SO_4 (99+%, Aldrich), and $Na_2B_4O_7 \cdot 10H_2O$ (Analytical Reagent grade, Mallinckrodt), KCN (97%, Aldrich) were used as received. H_2O with a resistivity >18.2 MΩ cm^{-1} (Barnsted Nanopure) was used throughout. Glass coated with a 400 nm fluorine-doped tin oxide layer (FTO, TEC 15, R_s < 12 Ω cm^{-1}, Pilkington) was used as support substrates. An n-type Ge(111) wafer section (miscut ≤ 0.5°, thickness = 0.5 mm, MTI Corporation) was used to collect comparative Raman spectra for bulk, crystalline Ge.

SERS-Active Au Nanoparticle Electrode Fabrication. FTO glass was cut into small rectangular sections, contacted with conductive Ag epoxy (CG Electronics), and then fixed onto a tinned Cu wire coil threaded through a 6 mm diameter glass tubing. The mounted substrates were insulated with an inert epoxy (1C Hysol, Loctite), exposing a conductive surface area of *ca.* 0.25 cm^2 (determined through computer-captured optical images and image analysis software). Electrodes were then rinsed sequentially with acetone and methanol, sonicated for 20 min in methanol, rinsed with solvent again, then dried under $N_2(g)$ before immediate immersion into a 10% v/v solution of $H_2N(CH_2)_3Si(OC_2H_5)_3$ in isopropyl alcohol for 48 h.[90] The Turkevich method[91] was used to prepare suspensions of Au nanoparticles through the reduction of aqueous $HAuCl_4$ by $Na_3C_6H_5O_7$ under reflux (size verified by UV—vis absorption, λ_{max} = 518 nm). After functionalization, each FTO electrode was immersed in an aqueous colloidal Au suspension for 12 h. Following, the coated FTO electrode was rinsed with H_2O and immersed in fresh colloidal Au suspension for another 12 h. This sequence was repeated again and resulted in film of Au nanoparticles that exhibited a detectable, albeit weak SERS enhancement. To increase the SERS activity of the Au nanoparticle films, the effective size of the adhered nanoparticles was increased through additional electroless plating of Au.[92] Each FTO substrate functionalized with Au nanoparticles was immersed in 10 mL of a stirred solution of 0.01 wt % $HAuCl_4$ to which 3 mL of 0.4×10^{-3} M NH_4OH was added over a course of 3 min. Electrodes were maintained in this stirred mixture for four additional minutes. Electrodes were then emersed, rinsed with H_2O, and dried under $N_2(g)$.

Physical Characterization. Scanning electron microscopic analysis of Au nanoparticle films was conducted with a FEI Nova Nanolab instrument operated at 5 kV with a secondary electron detector. X-ray diffraction spectra of the Au nanoparticle films were recorded with a Rigaku Ultima IV diffractometer with a Cu Kα source and acquired using a grazing angle geometry.

Electrochemical and Raman Spectral Analysis. All electrochemical data were collected with a CH Instruments 760C potentiostat. A single glass compartment, three-electrode cell was employed consisting of a Pt mesh and a Ag/AgCl (sat. KCl) electrode as the counter and reference electrodes respectively while a Au nanoparticle electrode served as the working electrode. An electrolyte of 0.5 M Na_2SO_4 and 0.01 M $Na_2B_4O_7$, pH 9.3, with and without 0.001 M GeO_2 was employed. Ar(g) was bubbled through all solutions for 20 min prior to the start of the measurements, and an Ar atmosphere was maintained above the solution layer in the cell during measurements.

Raman spectra were obtained using a Renishaw inVia Raman spectrometer equipped with a Leica microscope, an Olympus SLMPlan 20× objective (numerical aperture = 0.35), a RenCam CCD detector, a 1800 lines/mm grating, a 632.8 nm HeNe laser (Renishaw RL633), and a 514.5 nm Ar$^+$ laser (Laser Physics 25s). Spectra were acquired in a custom built Teflon cell containing 5 mL of electrolyte, Ag/AgCl (sat. KCl) reference, and Au coil counter electrodes. All reported spectra were collected using a total of 29 separately prepared samples and represent the average recorded response for samples prepared in the manner described above. Spectra were analyzed using the fitting routines included in the WiRE 3.1 software package.

Supporting Information Available: Details for true electrochemical surface area calculation, SERS enhancement factor determination, cyclic voltammetry, anodic stripping voltammetry, electrodeposition current—time transient analysis, irreversible potential-dependent crystalline order/disorder transitions, potential-dependent Raman spectra of adsorbed CN$^-$ at Au nanoparticle films, spectra acquired at varied power intensities, and information regarding estimation of the enhancement factors observed at Ge-coated SERS substrates are provided. This material is available free of charge *via* the Internet at http://pubs.acs.org.

REFERENCES AND NOTES

1. Nguyen, P.; Ng, H. T.; Meyyappan, M. Growth of Individual Vertical Germanium Nanowires. *Adv. Mater.* **2005,** *17,* 549–553.

2. Maeda, Y.; Tsukamoto, N.; Yazawa, Y.; Kanemitsu, Y.; Masumoto, Y. Visible Photoluminescence of Ge Microcrystals Embedded in SiO_2 Glassy Matrices. *Appl. Phys. Lett.* **1991,** *59,* 3168–3170.

3. Dashiell, M. W.; Denker, U.; Müller, C.; Costantini, G.; Manzano, C.; Kern, K.; Schmidt, O. G. Photoluminescence of Ultrasmall Ge Quantum Dots Grown by Molecular-Beam Epitaxy at Low Temperatures. *Appl. Phys. Lett.* **2002,** *80,* 1279–1281.

4. Niquet, Y. M.; Allan, G.; Delerue, C.; Lannoo, M. Quantum Confinement in Germanium Nanocrystals. *Appl. Phys. Lett.* **2000,** *77,* 1182–1184.

5. Colace, L.; Masini, G.; Assanto, G.; Luan, H.-C.; Wada, K.; Kimerling, L. C. Efficient High-Speed Near-Infrared Ge Photodetectors Integrated on Si Substrates. *Appl. Phys. Lett.* **2000,** *76,* 1231–1233.

6. Huang, Z.; Oh, J.; Campbell, J. C. Back-Side-Illuminated High-Speed Ge Photodetector Fabricated on Si Substrate Using Thin SiGe Buffer Layers. *Appl. Phys. Lett.* **2004,** *85,* 3286–3288.

7. King, R. R.; Law, D. C.; Edmondson, K. M.; Fetzer, C. M.; Kinsey, G. S.; Yoon, H.; Sherif, R. A.; Karam, N. H. 40% Efficient Metamorphic GaInP/GaInAs/Ge Multijunction Solar Cells. *Appl. Phys. Lett.* **2007,** *90,* 183516–183518.

8. Kanoun, M.; Souifi, A.; Baron, T.; Mazen, F. Electrical Study of Ge-Nanocrystal-Based Metal-Oxide-Semiconductor Structures for *p*-Type Nonvolatile Memory Applications. *Appl. Phys. Lett.* **2004,** *84,* 5079.

9. Bukhtiyarov, V. I.; Prosvirin, I. P.; Tikhomirov, E. P.; Kaichev, V. V.; Sorokin, A. M.; Evstigneev, V. V. *In Situ* Study of Selective Oxidation of Methanol to Formaldehyde Over Copper. *React. Kinet. Catal. Lett.* **2003,** *79,* 181–188.

10. Kaichev, V. V.; Prosvirin, I. P.; Bukhtiyarov, V. I. High-Pressure Studies of CO Adsorption on Pd(111) by X-ray Photoelectron Spectroscopy and Sum-Frequency Generation. *J. Phys. Chem. B* **2003,** *107,* 3522–3527.

11. Zhang, X.; Zhang, W.; Liu, L.; Sheen, Z. X. Surface-Enhanced Raman of Z-Vibration Mode in Single-Walled and Multi-walled Carbon Nanotube. *Chem. Phys. Lett.* **2003,** *372,* 497–502.

12. Yang, H.; Liu, Y.; Liu, Z.; Yang, Y.; Jiang, J.; Zhang, Z.; Shen, G.; Yu, R. Raman Mapping and *In Situ* SERS Spectroelectrochemical Studies of 6-Mercaptopurine SAMS on the Gold Electrode. *J. Phys. Chem. B* **2005,** *109,* 2739–2744.

13. Brown, G. M.; Hope, G. A. Confirmation of Thiourea/Chloride Ion Coadsoprtion at a Copper Electrode by *in Situ* SERS Spectroscopy. *J. Electroanal. Chem.* **1996,** *413,* 153–160.

14. Gao, P.; Weaver, M. J. Vibrational Coupling Effects for Cyanide and Aromatic Adsorbates at Gold Electrodes: A Comparative Study Using Surface Raman and Infrared Spectroscopies. *J. Phys. Chem.* **1989,** *93,* 6205–6211.

15. Gogotsi, Y.; Baek, C.; Kirscht, F. Raman Microspectroscopy Study of Processing-Induced Phase Transformations and Residual Stress in Silicon. *Semicond. Sci. Technol.* **1999,** *14,* 936–944.

16. Van Duyne, R. P.; Haushalter, J. P. Surface-Enhanced Raman Spectroscopy of Adsorbates on Semiconductor Electrode Surfaces: Tris(Bipyridine)Ruthenium(II) Adsorbed on Silver-Modified n-Gallium Arsenide(100). *J. Phys. Chem.* **1983,** *87,* 2999–3003.

17. Feng, Q.; Cotton, T. M. A Surface-Enhanced Resonance Raman Study of the Photoreduction of Methylviologen on a *p*-InP Semiconductor Electrode. *J. Phys. Chem. C* **1986,** *90,* 983–987.

18. Pettinger, B., *Tip-Enhanced Raman Spectroscopy (TERS)*; Springer-Verlag: Berlin, 2006; Vol. 103.

19. Li, J. F.; Huang, Y. F.; Ding, Y.; Yang, Z. L.; Li, S. B.; Zhou, X. S.; Fan, F. R.; Zhang, W.; Zhou, Z. Y.; Wu, D. Y.; *et al.* Shell-Isolated Nanoparticle-Enhanced Raman Spectroscopy. *Nature* **2010,** *464,* 392–395.

20. Gichuhi, A.; Boone, B. E.; Shannon, C. Resonance Raman Scattering and Scanning Tunneling Spectroscopy of CdS Thin Films Grown by Electrochemical Atomic-Layer Epitaxy—Thickness Dependent Phonon and Electronic Properties. *J. Electroanal. Chem.* **2002,** *522,* 21–25.

21. Yang, L.; Jiang, X.; Ruan, W.; Zhao, B.; Xu, W.; Lombardi, J. R. Observation of Enhanced Raman Scattering for Molecules Adsorbed on TiO₂ Nanoparticles: Charge-Transfer Contribution. *J. Phys. Chem. C* **2008,** *112,* 20095–20098.

22. Rossetti, R.; Beck, S. M.; Brus, L. E. Transient Raman Scattering Observations of Surface Reactions in Aqueous TiO₂ Colloids. *J. Am. Chem. Soc.* **1982,** *104,* 7322–7324.

23. Richter, A. P.; Lombardi, J. R.; Zhao, B. Size and Wavelength Dependence of Charge-Transfer Contributions to Surface-Enhanced Raman Spectroscopy in Ag/PATP/ZnO Junctions. *J. Phys. Chem. C* **2010,** *114,* 1610–1614.

24. Wang, Y.; Ruan, W.; Zhang, J.; Yang, B.; Xu, W.; Zhao, B.; Lombardi, J. R. Direct Observation of Surface-Enhanced Raman Scattering in ZnO Nanocrystals. *J. Raman Spectrosc.* **2009,** *40,* 1072–1077.

25. Musumeci, A.; Gosztola, D.; Schiller, T.; Dimitrijevic, N. M.; Mujica, V.; Martin, D.; Rajh, T. SERS of Semiconducting Nanoparticles (TiO₂ Hybrid Composites). *J. Am. Chem. Soc.* **2009,** *131,* 6040–6041.

26. Wang, Y.; Jia, H.; Li, M.; Zeng, J.; Yang, B.; Zhao, B.; Xu, W.; Lombardi, J. R. Mercaptopyridine Surface-Functionalized CdTe Quantum Dots with Enhanced Raman Scattering Properties. *J. Phys. Chem. C* **2008,** *112,* 996–1000.

27. Wang, Y.; Sun, Z.; Wang, Y.; Hu, H.; Zhao, B.; Xu, W.; Lombardi, J. R. Surface-Enhanced Raman Scattering on Mercaptopyridine-Capped CdS Microclusters. *Spectrochim. Acta, Part A* **2007,** *66,* 1199–1203.

28. Wang, Y.; Sun, Z.; Hu, H.; Jing, S.; Zhao, B.; Xu, W.; Zhao, C.; Lombardi, J. R. Raman Scattering Study of Molecules Adsorbed on ZnS Nanocrystals. *J. Raman Spectrosc.* **2007,** *38,* 34–38.

29. Wang, Y.; Hu, H.; Jing, S.; Wang, Y.; Sun, Z.; Zhao, B.; Zhao, C.; Lombardi, J. R. Enhanced Raman Scattering as a Probe for 4-Mercaptopyridine Surface-Modified Copper Oxide Nanocrystals. *Anal. Sci.* **2007,** *23,* 787–791.

30. Sun, Z.; Zhao, B.; Lombardi, J. R. ZnO Nanoparticle Size-Dependent Excitation of Surface Raman Signal from Adsorbed Molecules: Observation of a Charge-Transfer Resonance. *Appl. Phys. Lett.* **2007,** *91,* 221106–1−3.

31. Zhang, P.; Wang, Y.; He, T.; Zhang, B.; Wang, X.; Xin, H.; Liu, F.-c. SERS of Pyridine, 1,4-Dioxane and 1-Ethyl-3′-methyl-2-thiacyanine Iodide Adsorbed on A-Fe₂O₃ Colloids. *Chem. Phys. Lett.* **1988,** *153,* 215.

32. Livingstone, R.; Zhou, X.; Tamargo, M. C.; Lombardi, J. R.; Quagliano, L. G.; Jean-Mary, F. Surface Enhanced Raman Spectroscopy of Pyridine on CdSe/ZnBeSe Quantum Dots Grown by Molecular Beam Epitaxy. *J. Phys. Chem. C* **2010,** *114,* 17460–17464.

33. Weaver, M. J.; Zou, S.; Chan, H. Y. The New Interfacial Ubitquity of Surface-Enhanced Raman Spectroscopy. *Anal. Chem.* **2000,** *72,* 38A–47A.

34. Wasileski, S. A.; Zou, S.; Weaver, M. J. Surface-Enhanced Raman Scattering from Substrates with Conducting or Insulator Overlayers: Electromagnetic Model Predictions and Comparison with Experiment. *Appl. Spectrosc.* **2000,** *54,* 761–772.

35. Zou, S.; Weaver, M. J. Potential-Dependent Metal-Adsorbate Stretching Frequencies for Carbon Monoxide on Transition-Metal Electrodes: Chemical Bonding *versus* Electrostatic Field Effects. *J. Phys. Chem.* **1996,** *100,* 4237–4242.

36. Zou, S.; Weaver, M. J. Surface-Enhanced Raman Scattering of Ultrathin Cadmium Chalcogenide Films on Gold Formed by Electrochemical Atomic-Layer Epitaxy: Thickness-Dependent Phonon Characteristics. *J. Phys. Chem. B* **1999,** *103,* 2323–2326.

37. Zou, S.; Weaver, M. J. Surface-Enhanced Raman Spectroscopy of Cadmium Sulfide/Cadmium Selenide Superlattices Formed on Gold by Electrochemical Atomic-Layer Epitaxy. *Chem. Phys. Lett.* **1999,** *312,* 101–107.

38. Thompson, W. R.; Pemberton, J. E. Raman Spectroscopy of Covalently Bonded Alkylsilane Layers on Thin Silica Films Immobilized on Silver Substrates. *Anal. Chem.* **1994,** *66,* 3362–3370.

39. Lacy, W. B.; Williams, M. J.; Wenzler, L. A.; Beebe, T. P.; Harris, J. M. Characterization of SiO₂-Overcoated Silver-Island Films as Substrates for Surface-Enhanced Raman Scattering. *Anal. Chem.* **1996,** *68,* 1003–1011.

40. Park, S.; Yang, P.; Corredor, P.; Weaver, M. J. Transition Metal-Coated Nanoparticle Films: Vibrational Characterization with Surface-Enhanced Raman Scattering. *J. Am. Chem. Soc.* **2002,** *124,* 2428–2429.

41. McFarland, A. D.; Young, M. A.; Dieringer, J. A.; Van Duyne, R. P. Wavelength-Scanned Surface-Enhanced Raman Excitation Spectroscopy. *J. Phys. Chem. B* **2005,** *109*, 11279–11285.

42. Pourbaix, M. *Atlas of Electrochemical Equilibria in Aqueous Solutions*; 1st ed.; Pergamon Press: Oxford, 1966.

43. Liang, X.; Kim, Y.-G.; Geberziabiher, D. K.; Stickney, J. L. Aqueous Electrodeposition of Ge Monolayers. *Langmuir* **2010,** *26*, 2877–2884.

44. J. H. Parker, J.; Feldman, D. W.; Ashkin, M. Raman Scattering by Silicon and Germanium. *Phys. Rev.* **1967,** *155*, 712–714.

45. Weinstein, B. A.; Cardona, M. Second-Order Raman Spectrum of Germanium. *Phys. Rev. B* **1973,** *7*, 2545–2551.

46. Gaĭsler, V. A.; Neizvestnyĭ, I. G.; Sinyukov, M. P.; Talochkin, A. B. Raman Scattering by Surface Vibrations of Germanium Crystals. *JETP Lett.* **1987,** *45*, 441–444.

47. Fortner, J.; Yu, R. Q.; Lannin, J. S. Near-Surface Raman Scattering in Germanium Clusters and Ultrathin Amorphous Films. *Phys. Rev. B* **1990,** *42*, 7610–7613.

48. Lannin, J. S.; Maley, N. Raman Scattering and Short Range Order in Amorphous Germanium. *Solid State Commun.* **1985,** *53*, 939–942.

49. Wihl, M.; Cardona, M.; Tauc, J. Raman Scattering in Amorphous Ge and III—V Compounds. *J. Non-Cryst. Solids* **1972,** *8—10*, 172–178.

50. Watling, K.; Hope, G. A.; Woods, R. SERS Investigation of Gold Dissolution in Chloride and Cyanide Media. *J. Electrochem. Soc.* **2005,** *152*, D103–D108.

51. Beltramo, G. L.; Shubina, T. E.; Mitchell, S. J.; Koper, M. T. M. Cyanide Adsorption on Gold Electrodes: A Combined Surface Enhanced Raman Spectroscopy and Density Functional Theory Study. *J. Electroanal. Chem.* **2004,** *563*, 111–120.

52. Murray, C. A.; Bodoff, S. Cyanide Adsorption on Silver and Gold Overlayers on Island Films as Determined by Surface Enhanced Raman Scattering. *J. Chem. Phys.* **1986,** *85*, 573–584.

53. Maroun, F.; Ozanam, F.; Chazalviel, J.-N. *In Situ* Infrared Monitoring of Hydrogen Adsorption/Desorption at a Germanium Electrode. *Surf. Sci.* **1999,** *427—428*, 184–189.

54. Bermejo, D.; Cardona, M. Raman Scattering in Pure and Hydrogenated Amorphous Germanium and Silicon. *J. Non-Cryst. Solids* **1979,** *32*, 405–419.

55. Rivillon, S.; Chabal, Y. J.; Amy, F.; Khan, A. Hydrogen Passivation of Germanium (100) Surface Using Wet Chemical Preparation. *Appl. Phys. Lett.* **2005,** *87*, 253101-1–253101-3.

56. Chabal, Y. J. High-Resolution Infrared Spectroscopy of Adsorbates on Semiconductor Surfaces: Hydrogen on Si(100) and Ge(100). *Surf. Sci.* **1986,** *168*, 594–608.

57. Maroun, F.; Ozanam, F.; Chazalviel, J.-N. *In Situ* Infrared Monitoring of Electrochemical Adsorption/Desorption of Hydrogen on Germanium. *Chem. Phys. Lett.* **1998,** *292*, 493–499.

58. Henderson, G. S.; Fleet, M. E. The Structure of Glasses Along the $Na_2O—GeO_2$ Join. *J. Non-Cryst. Solids* **1991,** *134*, 259.

59. Liu, Y.; Shimizu, M.; Wang, X.; Zhu, B.; Sakakura, M.; Shimotsuma, Y.; Qiu, J.; Miura, K.; Hirao, K. Confocal Raman Imaging of Femtosecond Laser Induced Microstructures in Germanate Glasses. *Chem. Phys. Lett.* **2009,** *477*, 122–125.

60. Walrafen, G. E. Raman Spectral Studies of Alkaline Solutions of Germanium Dioxide. *J. Chem. Phys.* **1965,** *42*, 485–492.

61. Giacomazzi, L.; Umari, P.; Pasquarello, A. Medium-Range Structural Properties of Vitreous Germania Obtained through First-Principles Analysis of Vibrational Spectra. *Phys. Rev. Lett.* **2005,** *95*, 075505–1—4.

62. Henderson, G. S.; Bancroft, G. M.; Fleet, M. E. Raman Spectra of Gallium and Germanium Substituted Silicate Glasses: Variations in Intermediate Range Order. *Am. Mineral.* **1985,** *70*, 946–960.

63. Henderson, G. S.; Wang, H. M. Germanium Coordination and the Germanate Anomaly. *Eur. J. Mineral* **2002,** *14*, 733–744.

64. Hass, M. Raman Spectra of Vitreous Silica, Germania and Sodium Silicate Glasses. *J. Phys. Chem. Solids* **1970,** *31*, 415–422.

65. Scott, J. F. Raman Spectra of GeO_2. *Phys. Rev. B* **1970,** *1*, 3488–3493.

66. Yadav, H. K.; Sreenivas, K.; Katiyar, R. S.; Gupta, V. Defect Induced Activation of Raman Silent Modes in RF Co-sputtered Mn Doped ZnO Thin Films. *J. Phys. D: Appl. Phys.* **2007,** *40*, 6005–6009.

67. Moskovits, M. Surface Selection Rules. *J. Phys. Chem.* **1982,** *77*, 4408–4416.

68. Gao, X.; Davies, J. P.; Weaver, M. J. A Test of Surface Selection Rules for Surface-Enhanced Raman Scattering: The Orientation of Adsorbed Benzene and Monosubstituted Benzenes on Gold. *J. Phys. Chem.* **1990,** *94*, 6858–6864.

69. Leite, R. C. C.; Porto, S. P. S. Enhancement of Raman Cross Section in CdS Due to Resonant Absorption. *Phys. Rev. Lett.* **1966,** *17*, 10–12.

70. Leite, R. C. C.; Scott, J. F. Resonant Surface Raman Scattering in Direct-Gap Semiconductors. *Phys. Rev. Lett.* **1969,** *22*, 130–132.

71. Nishimura, Y.; Fukunaka, Y. Electrochemical Reduction of Silicon Chloride in a Nonaqueous Solvent. *Electrochim. Acta* **2007,** *53*, 111–116.

72. Tauc, J.; Abrahám, A.; Zallen, R.; Slade, M. Infrared Absorption in Amorphous Germanium. *J. Non-Cryst. Solids* **1970,** *4*, 279–288.

73. Campbell, I. H.; Fauchet, P. M. The Effects of Microcrystal Size and Shape on the One Phonon Raman Spectra of Crystalline Semiconductors. *Solid State Commun.* **1986,** *58*, 739–741.

74. Richter, H.; Wang, Z. P.; Ley, L. The One Phonon Raman Spectrum in Microcrystalline Silicon. *Solid State Commun.* **1981,** *39*, 625–629.

75. Rolo, A. G.; Vasilevskiy, M. I. Raman Spectroscopy of Optical Phonons Confined in Semiconductor Quantum Dots and Nanocrystals. *J. Raman Spectrosc.* **2007,** *38,* 618–633.

76. Markov, I. Saturation Nucleus Density in the Electrodeposition of Metals onto Inert Electrodes I. Theory. *Thin Solid Films* **1976,** *35*, 11–20.

77. Hills, G. J.; Schiffrin, D. J.; Thompson, J. Electrochemical Nucleation from Molten Salts I. Diffusion Controlled Electrodeposition of Silver from Alkali Molten Nitrates. *Electrochim. Acta* **1974,** *19*, 657–670.

78. Gerischer, H.; Mauerer, A.; Mindt, W. Nachweis einer Intermediären Radikalstruktur der Germanium-Oberfläche Beim Ubergang Zwischen Hydrid- ud Hydroxidbelegung. *Surf. Sci.* **1966,** *4*, 431–439.

79. Choi, K.; Buriak, J. M. Hydrogermylation of Alkenes and Alkynes on Hydride-Terminated Ge(100) Surfaces. *Langmuir* **2000,** *16*, 7737–7741.

80. Cullen, G. W.; Amick, J. A.; Gerlich, D. The Stabilization of Germanium Surfaces by Ethylation: II. Chemical Analysis. *J. Electrochem. Soc.* **1962,** *109*, 127–132.

81. Cullen, G. W.; Amick, J. A.; Gerlich, D. The Stabilization of Germanium Surfaces by Ethylation. I. Chemical Treatment. *J. Electrochem. Soc.* **1962,** *109*, 124–127.

82. Ardalan, P.; Sun, Y.; Pianetta, P.; Musgrave, C. B.; Bent, S. F. Reaction Mechanism, Bonding, and Thermal Stability of 1-Alkanethiols Self-Assembled on Halogenated Ge Surfaces. *Langmuir* **2010,** *26*, 8419–8429.

83. Ye, J. H.; Pan, J. S.; Liu, J. G.; Li, S. F. Y. Reversible Phase Transformation on Ge(111) Surface by Potential. *Electrochem. Solid-State Lett.* **1999,** *2*, 448–451.

84. Kepler, K. D.; Gewirth, A. A. *In Situ* AFM and STM Investigation of Electrochemical Hydride Growth on Ge(110) and Ge(111) Surfaces. *Surf. Sci.* **1994,** *303*, 101–113.

85. Amy, S. R.; Chabal, Y. J. Passivation and Characterization of Germanium Surfaces. In *Advanced Gate Stacks for High-Mobility Semiconductors*; Dimoulas, A., Gusev, E., McIntyre, P. C., Hyens, M., Eds.; Springer: Berlin, 2007.

86. Lewis, L. N.; Litz, K. E.; Anostario, J. M. Direct Formation of Ge—C Bonds from GeO_2. *J. Am. Chem. Soc.* **2002,** *124*, 11718–11722.

87. Chen, X.; Cai, Q.; Wang, W.; Mo, G.; Jiang, L.; Zhang, K.; Chen, Z.; Wu, Z.; Wu, Z. Formation of Ge—S Bonds from AOT-Coated GeO$_2$ Nanoparticles at High Temperature: An *In Situ* Heating EXAFS Investigation. *Chem. Mater.* **2008,** *20*, 2757–2762.

88. Hamers, R. J.; Coulter, S. K.; Ellison, M. D.; Hovis, J. S.; Padowitz, D. F.; Schwartz, M. P.; Greenlief, C. M.; John N. Russell, J. Cycloaddition Chemistry of Organic Molecules with Semiconductor Surfaces. *Acc. Chem. Res.* **2000,** *33*, 617–624.

89. Lewis, L. N.; Schattenmann, F. J.; Jordan, T. M.; Carnahan, J. C.; Flanagan, W. P.; Wroczynski, R. J.; Lemmon, J. P.; Anostario, J. M.; Othon, M. A. Reaction of Silicate Minerals to Form Tetramethoxysilane. *Inorg. Chem.* **2002,** *41*, 2608–2615.

90. Musick, M. D.; Keating, C. D.; Lyon, L. A.; Botsko, S. L.; Peña, D. J.; Holliway, W. D.; McEvoy, T. M.; Richardson, J. N.; Natan, M. J. Metal Films Prepared by Stepwise Assembly. 2. Construction and Characterization of Colloidal Au and Ag Multilayers. *Chem. Mater.* **2000,** *12*, 2869–2881.

91. Turkevich, J.; Stevenson, P. C.; Hillier, J. A Study of the Nucleation and Growth Processes in the Synthesis of Colloidal Gold. *Discuss. Faraday. Soc.* **1951,** *11*, 55–75.

92. Brown, K. R.; Lyon, A.; Fox, A. P.; Reiss, B. D.; Natan, M. J. Hydroxylamine Seeding of Colloidal Au Nanoparticles. 3. Controlled Formation of Conductive Au Films. *Chem. Mater.* **2000,** *12*, 314–323.